Check for updates

Water Science & Technology

IWA PUBLISHING

© 2021 The Authors

Water Science & Technology Vol 84 No 1, 159 doi: 10.2166/wst.2021.221

Fe_3O_4-NPs/orange peel composite as magnetic heterogeneous Fenton-like catalyst towards high-efficiency degradation of methyl orange

Qiang Zhao, Congcong Zhang, Xiaoqiang Tong, Yunling Zou, Yan Li and Fang Wei*
College of Science, Civil Aviation University of China (CAUC), Tianjin, 300300, China
*Corresponding author. E-mail: f_wei@cauc.edu.cn

QZ, 0000-0002-2545-2383; FW, 0000-0003-4462-0562

ABSTRACT

Magnetite nanoparticles (Fe_3O_4-NPs)/orange peel (MOP) composite was prepared via one-step in-situ co-precipitation method as magnetic heterogeneous Fenton-like catalyst. The properties of MOP were characterized by scanning electron microscopy, transmission electron microscopes, Brunauer–Emmett–Teller, X-ray diffraction, Fourier-transform infrared, thermogravimetric analysis and X-ray photoelectron spectroscopy technologies. Its Fenton-like catalytic responses towards removal of methyl orange (MO) were investigated, in which the effects of initial dye concentration, pH, temperature and hydrogen peroxide dosage were studied. The MO degradation ratio up to 98.0% was obtained within 20 min in optimized conditions. The catalyst showed excellent catalytic stability exhibiting nearly 90% degradation ratio in the 10th cycle within 20 min, whereas pure Fe_3O_4-NPs showed only 62.5% in this stage. Due to the stabilization of complexing orange peel hydroxyl to iron oxide in the composite and its magnetic separation property, MOP composite exhibits excellent Fenton-like catalytic performance, which offers great prospects for low-cost and high-efficiency organic dye wastewater treatment.

Key words: catalysis, catalyst reuse, composite, heterogeneous Fenton-like catalyst, magnetic, thermogravimetric analysis

HIGHLIGHTS

- Cheap raw materials like waste biomass and common Fe salts.
- Fe_3O_4/orange peel composite as heterogeneous Fenton-like catalyst.
- 98.0% of 30 ppm MO can be degraded within 20 min in optimized conditions.
- Easy separation: fast magnetic separation from aqueous solution within 1 min.
- Superior cycle catalytic stability: MO (20 ppm) degradation ratio reaches up to nearly 90% within 20 min in the 10th cycle.

GRAPHICAL ABSTRACT

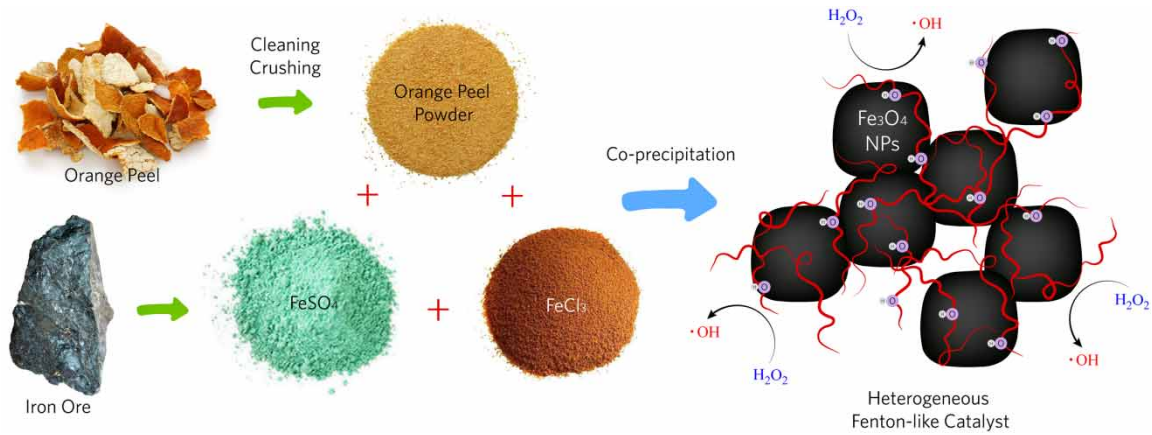

This is an Open Access article distributed under the terms of the Creative Commons Attribution Licence (CC BY 4.0), which permits copying, adaptation and redistribution, provided the original work is properly cited (http://creativecommons.org/licenses/by/4.0/).

Downloaded from http://iwaponline.com/wst/article-pdf/84/1/159/913098/wst084010159.pdf
by guest

INTRODUCTION

Industrial water pollution is a serious threat to ecological environment and human health at present (Wang & Yang 2016; Naushad *et al.* 2019b; Alqadami *et al.* 2020; Khan *et al.* 2020). Wastewater from the printing and dyeing has large amounts of azo dyes like methyl orange (MO), which has metabolites that are often carcinogenic, teratogenic, mutagenic and biotoxic to living organisms (Jia *et al.* 2019). A number of recent studies on the removal of water polutants have been carried out, including biodegradation (Oliveira *et al.* 2020), physical adsorption (Ali *et al.* 2018; Ali *et al.* 2019; Naushad *et al.* 2019a; Abdul-Hameed & Al Juboury 2020; Al Juboury & Abdul-Hameed 2019), and catalytic oxidation or reduction degradation (Ahsan *et al.* 2019a, 2019b, 2019c, 2020a). Among them, advanced oxidation processes, including UV–visible photolysis oxidation, catalytic wet air oxidation, ozone oxidation, electrochemical oxidation and Fenton oxidation, are considered to be a promising approach for the removal of refractory and toxic organic dyes (Chan *et al.* 2011; Tijani *et al.* 2014; Deng & Zhao 2015; Cheng *et al.* 2016; Ahsan *et al.* 2021). In Fenton oxidation, the strong oxidizing hydroxyl radicals (·OH, $E_{ox} = 2.80$ V) and hydroxyl oxygen radicals (·OOH, $E_{ox} = 1.70$ V) can be generated from decomposition of hydrogen peroxide (H_2O_2) in the presence of ferrous ions (Fe^{2+}) (Babuponnusami & Muthukumar 2014). The advantage of the low cost and high reliability of Fenton processes is that organic dye molecules like MO, can be completely mineralized to carbon dioxide (CO_2) and water (H_2O) in moderate conditions (Youssef *et al.* 2016). However, the classic homogeneous Fenton process has several disadvantages like a narrow pH range and the production of a large amount of iron sludge. To overcome these limitations, both non-iron transition metal-based and iron-based catalysts for heterogeneous Fenton-like system have been investigated (Ahsan *et al.* 2020b, 2020c). Iron-based heterogeneous Fenton-like catalyst is abundant in nature and can potentially be used for large-scale industrial dyeing wastewater treatment.

Specifically, magnetite (Fe_3O_4) nanoparticles (NPs) with Fe(II) and Fe(III) active sites have been good candidates for heterogeneous Fenton-like catalysts, because they are high-efficient and low-cost and can separate solid-state catalyst from the treated effluent with less post-treatment of ferric hydroxide ($Fe(OH)_3$) sludge (Zhang *et al.* 2009; Adyani & Soleimani 2019; Zheng *et al.* 2019). Nanoscaled Fe_3O_4 with high surface/volume ratio can effectively enhance the reaction kinetics influenced by limited contact between reactant and catalyst in conventional heterogeneous Fenton-like systems (Wan *et al.* 2016). However, the magnetite NPs catalyst tends to aggregate and leach Fe element during multiple catalytic cycles due to its high surface energy and reaction activity, which reduces its Fenton catalytic performance (Tang & Wang 2018).

To overcome these drawbacks, the surface modification strategy to magnetic NPs can be adapted to change their surface states (Li *et al.* 2020). Some agents like organic acid derivatives (Wei *et al.* 2012; Fan *et al.* 2016) and silicate esters/organic amine (Abboud *et al.* 2015; Jia *et al.* 2019), polymer precursors (Abboud *et al.* 2015; Gamallo *et al.* 2018) and surfactants (Angamuthu *et al.* 2017) have been used to change the surface chemical groups of magnetite NPs or form a core-shell or yolk-shell structure (Cui *et al.* 2013; Lv *et al.* 2014; Du *et al.* 2017) so that the modified magnetite NPs can be stabilized instead of agglomerated. Although the developed Fenton-like catalyst can be obtained via surface modification technology towards higher catalytic efficiency at near neutral pH and more stable catalytic activity compared to nanoscaled Fe_3O_4, the corresponding preparation processes have been expensive and complex.

In the past few years, agricultural wastes and biomass residues have caused severe environmental problems due to their high chemical oxygen demand leading to the depletion of oxygen in natural water. After appropriate chemical treatment, these biomass sources become promising renewable carbon-rich materials (Titirici *et al.* 2007), which are widely used to produce low-cost biochar or their derivatives as absorbents due to the attainable porous structure and abundant surface groups (Chen *et al.* 2011; Gupta & Nayak 2012; Tan *et al.* 2016; Zou *et al.* 2016). One of the agricultural wastes from orange juice industry is orange peel (OP), which mainly consists of cellulose, hemicellulose, pectin (galacturonic acid), lignin and other low molecular weight compounds (Zapata *et al.* 2009). Abundant hydroxyl groups contribute to the anchoring effect for dispersing Fe oxide NPs in OP structure (Lafi *et al.* 2015; Shehzad *et al.* 2018), which makes it a low-cost and sustainable approach to developing a stable heterogeneous Fenton-like catalyst. Therefore, due to the enhanced stabilization of magnetite by OP, it can be used to reduce the reduction of Fe content in the catalyst during the Fenton-like process.

In this work, Fe_3O_4-NPs/OP composite (MOP) was developed in a one-step reaction to evaluate its feasibility as heterogeneous Fenton-like catalyst for the degradation of MO. After detailed characterization, the Fenton-like degradation of MO promoted by MOP in different conditions was performed to evaluate its catalytic reactivity, stability and separation properties. The reuse performance was also investigated during several catalytic cycles. MOP is a robust, high-efficiency Fenton-like catalyst with a very low-cost synthesis method in water treatment application.

Downloaded from http://iwaponline.com/wst/article-pdf/84/1/159/913098/wst084010159.pdf
by guest

MATERIALS AND METHODS

Materials

MO dye was purchased from Beijing Innochem Science & Technology Co., Ltd. Hydrogen peroxide (analytically pure (AR), ~ 30%) was provided by Shanghai Experiment Reagent Co., Ltd. Ethanol (analytically pure (AR), ~ 99.7%), chloroform (AR, ~ 99.0%), hydrogen chloride (AR, ~ 36%), ammonium hydroxide (AR, ~ 26%), ferric trichloride, hexahydrate ($FeCl_3 \cdot 6H_2O$, AR, ~ 99.0% and ferrous sulfate, heptahydrate $FeSO_4 \cdot 7H_2O$, AR, ~ 98%) were purchased from Sinopharm Chemical Reagent Co., Ltd. Oranges were purchased from a local market. All the chemicals were used directly without further purification, and solutions were prepared with deionized water produced in our laboratory.

Preparation of Fenton-like catalyst

The OP was sliced into small pieces and washed with deionized water twice, then dried in an air-oven at 70 °C. These dry orange pieces were crushed into a powder which was filtered through 60 mesh screen (denoted as OP).

MOP was synthesized by co-precipitation method according to Gupta (Gupta & Nayak 2012), which was slightly modified. Briefly, 6.1 g $FeCl_3 \cdot 6H_2O$ and 4.2 g of $FeSO_4 \cdot 7H_2O$ were dissolved in 100 mL water and heated to 90 °C in a round-bottomed flask. Then, 1 g OP powder was directly added into this flask. The mixture of 10 mL of ammonium hydroxide (26%) and 100 mL of water was prepared and dropwise added into the flask. The pH of the reaction system was adjusted to 10. The mixture was continuously stirred at 80 °C for 30 min and then cooled to room temperature naturally. The black precipitate MOP was separated by centrifugation at 10,000 rpm for 10 min, washed to neutral pH with deionized water, dried at 50 °C for 24 h and finally stored in a centrifuge tube for further use. The pure Fe_3O_4-NPs (denoted as MP) were also prepared in a similar way without adding OP powder.

Characterization methods

The products were characterized by scanning electron microscopy (SEM, JEOL-6701) and transmission electron microscopy (TEM; Tecnai G2 F30 S-TWIN) for morphology research. The specific surface area was calculated using Brunauer–Emmett–Teller (BET) method and obtained on ASAP 2,460 by N_2 adsorption–desorption method. X-ray diffraction (XRD) patterns were performed on DX-2700BH with Cu k_α radiation at 30 kV and 25 mA. Fourier-transform infrared (FT-IR) spectra were recorded in the 4,000–400 cm^{-1} region by Nicolet Avatar 330 FT-IR at room temperature. The thermogravimetric analysis (TGA) was performed on SDT-Q600 at temperatures ranging from room temperature to 800 °C at a heating rate of 10 °C min^{-1} in air. The precise chemical composition of MOP was determined by inductively coupled plasma optical emission spectroscopy (ICPOES730, Agilent). The X-ray photoelectron spectroscopy (XPS) was measured using Thermo ESCALAB 250xi. The magnetic property of MOP was evaluated using a Quantum Design superconducting quantum interference device (SQUID VSM). The degradation of MO was monitored by the change of absorbance at maximum absorption wavelength using UV–visible spectrophotometer (UVmini-1240, Shimadzu).

Catalytic removal of MO

The heterogeneous Fenton-like catalytic reaction was evaluated by the degradation of MO. In a typical catalytic cycle, the reaction suspensions were prepared by adding a given amout of catalyst MOP (25 mg for catalyst concentration of 1 g/L) into a 50 mL centrifuge tube with 25 mL MO solution. The mixture was stirred and heated in a water bath at a specific temperature prior to adding H_2O_2 (2 mL, 30%). Concentration samplings were taken at given time intervals during the reaction. The MOP catalyst was separated by applying magnetic field and the absorption sepctra of the supernatant MO solution was recorded at the maximum absorption wavelength. Meanwhile, the recovered catalyst was washed and purified with deionized water. After that, the recovered MOP catalyst was collected for cyclic use.

RESULTS AND DISCUSSION

Characterization results

SEM and TEM photographs present the morphological characteristics of OP, MP and MOP. Figure 1(a) shows that OP has a complex structured surface morphology with numerous wrinkles. The energy-dispersive spectroscopy (EDS) analysis confirms that OP consists of abundant carbon, hydrogen, oxygen and little nitrogen, sulfur, potassium and calcium (Figure A.1 and Table A.1, supplementary data) (Siles *et al.* 2016). According to TEM images of the prepared MP in Figure 1(b) and 1(c), MP is presented as NPs with average size of 14.72 nm (Figure A.3a). Compared with OP, MOP possesses distinct surface morphology

Downloaded from http://iwaponline.com/wst/article-pdf/84/1/159/913098/wst084010159.pdf
by guest

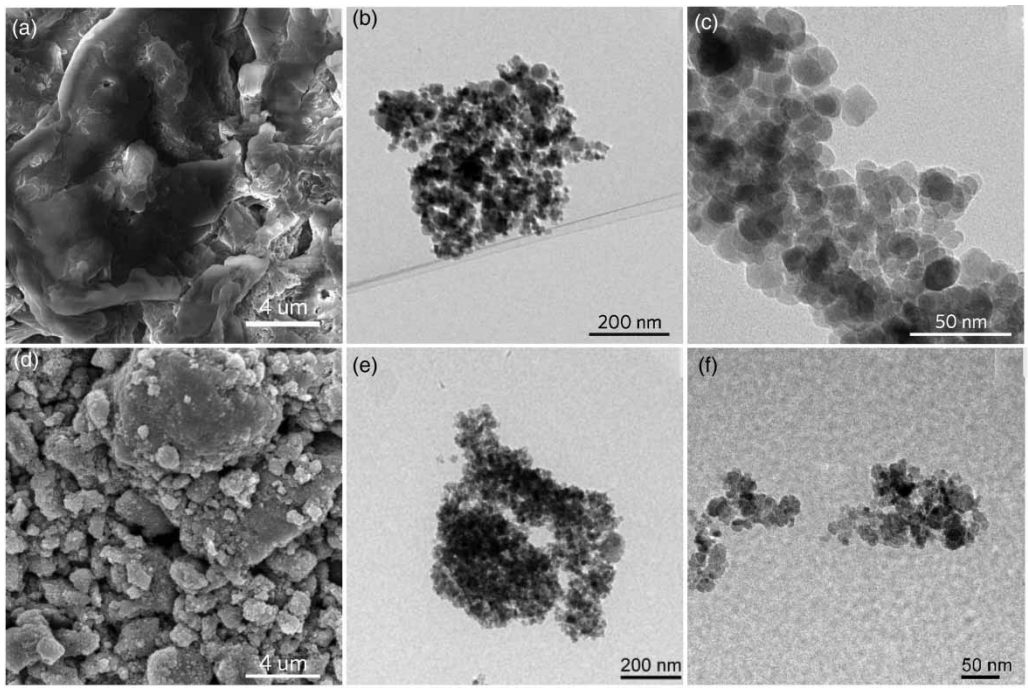

Figure 1 | (a) SEM image of OP, (b) and (c) TEM images of MP, (d) SEM image of MOP, (e) and (f) TEM images of MOP.

with more roughness according to the SEM image illustrated in Figure 1(d), which is attributed to Fe_3O_4-NPs on its surface (see EDS analysis in Figure A.2 and Table A.2). Unlike the smooth surface of Fe_3O_4-NPs, TEM images of MOP show its rough surface and blurred grain boundaries due to the complexation of OP component (surface hydroxyl groups) in MOP according to Figure 1(e) and 1(f). The Fe_3O_4 grain size is approximately 15.59 nm by average (Figure A.3b). The BET specific surface area of MOP is 57.73 m^2/g (Figure A.4a), whereas BET surface of OP is 1.53 m^2/g (Figure A.4b) and that of MP is 54.61 m^2/g (Figure A.4c). The N_2 adsorption–desorption isotherms of MOP show a type IV curve with a H3 hysteresis loop, which is the same as MP (see Figure A.4d and A.4e). The Barrett–Joyner–Halenda results indicate that both MOP and MP have the characteristics of mesoporous materials with the most probable pore diameter calculated from the desorption branch being 8.44 nm (Figure A.4d) and 3.02 nm (Figure A.4e), respectively. To be specific, MP also has macropores with diameter distribution ranging from 20 to 60 nm, which is attributed to the gaps among the Fe_3O_4-NPs.

XRD patterns of the OP, MP and MOP are shown in Figure 2. The extra broad scattering peak at low diffraction angle range is attributed to the amorphous state of SiO_2 substrate. The XRD pattern of OP does not show any distinct peak, which indicates its non-crystal nature (Khan *et al.* 2019a). The characteristic peaks for MOP and MP at 30.3°, 35.7°, 43.4°, 53.9°, 57.5°

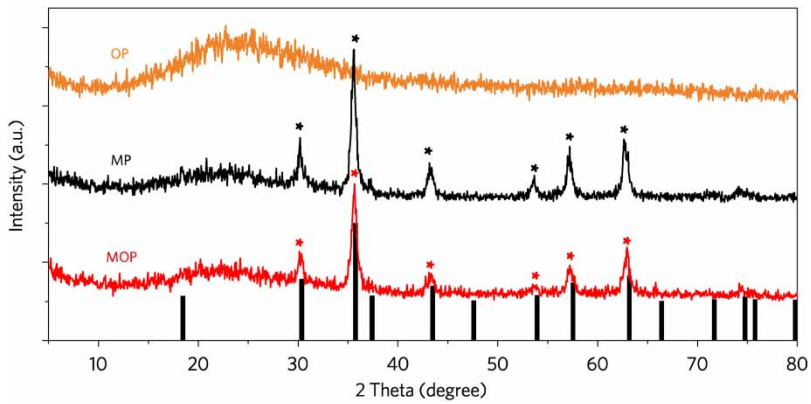

Figure 2 | XRD patterns of OP, MP, MOP and JCPDS no. 75-0449 (magnetite).

Downloaded from http://iwaponline.com/wst/article-pdf/84/1/159/913098/wst084010159.pdf
by guest

and 63.1° are identical to crystal plane index (220), (331), (400), (422), (511) and (440) of Fe_3O_4 according to JCPDS no. 75-0449 standard XRD pattern of Fe_3O_4. These results reveal that MOP involves Fe_3O_4 with inverse-spinel structure (Gupta & Nayak 2012), indicating that the OP complexing effect in MOP causes no change in the phase of Fe_3O_4 by co-precipitation method.

The mean crystallite size (D) of Fe_3O_4 is estimated by applying the Debye–Scherrer equation as depicted in Equation (1) (Holzwarth & Gibson 2011):

$$D_{hkl} = \frac{k\lambda}{\beta_{hkl} \cos \theta} \tag{1}$$

where D_{hkl} is the crystallite size in the direction perpendicular to the lattice planes, k is the Debye–Scherrer constant referring to the crystallite-shape factor (0.89), λ is the X-ray wavelength (0.15406 nm), β_{hkl} is the radian value of full width at half maximum intenstiy of the diffration peak, and θ is the diffraction angle. The mean crystallite sizes of magnetite nanocrystalline of MOP and MP in the direction perpendicular to the lattice plane are calculated as shown in Table A.3. The calculated D_{331} of MP is 14.1 nm (average) and of MOP is 16.1 nm (average), which is similar to the static average sizes of MP and MOP according to their TEM images (Figure A.3).

The FT-IR spectra of OP, MP and MOP are shown in Figure 3, and the vibration absorption peak positions of the main functional groups are depicted as follows: –OH (absorption peak at 3,000–3,600 cm^{-1}), C–H (absorption peaks at 2,939 and 1,384 cm^{-1}), ester C = O (absorption peak at 1,743 cm^{-1}), aromatic C = C (absorption peak at 1,651 cm^{-1}), C–O–C (absorption peak at 1,071 cm^{-1}). The broad and intense absorption peak at 3,418 cm^{-1} corresponds to the O–H stretching vibrations of cellulose, hemicellulose, pectin, lignin and absorbed water. The peaks observed at 2,939 cm^{-1} and 1,384 cm^{-1} can be attributed to C–H stretching and bending vibrations of methyl, methylene and methoxy groups. The

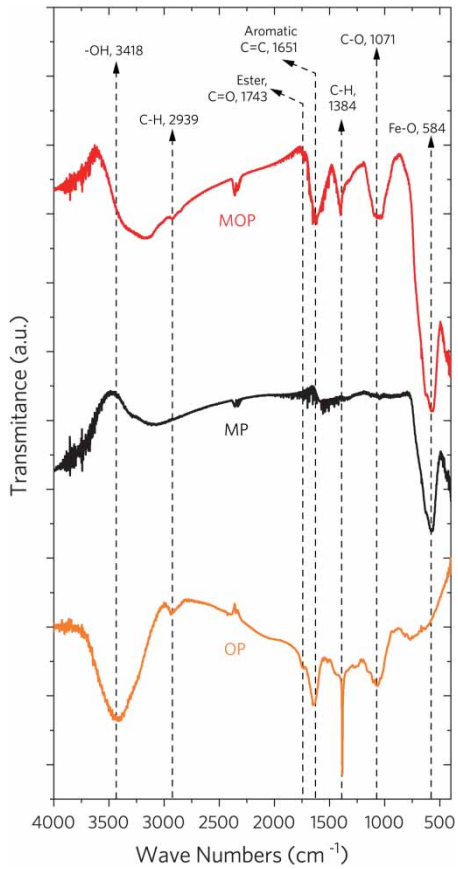

Figure 3 | FT-IR spectra of OP, MP and MOP.

Downloaded from http://iwaponline.com/wst/article-pdf/84/1/159/913098/wst084010159.pdf
by guest

peak at 1,743 cm^{-1} is the stretching vibration of C = O bond due to non-ionic carboxyl groups (–COOH, $–COOCH_3$), and may be assigned to carboxylic acids or esters in pectin (Feng *et al.* 2011). The peak at 1,651 cm^{-1} can be assigned to the C = C bond of benzene ring structure in lignin. The peak at 1,071 cm^{-1} refers to the glycosidic bond (C-O-C) mainly existing in cellulose, hemicellulose and pectin (Khan *et al.* 2019b). As a result, MOP retains most of the functional groups of OP due to its in-situ co-precipitation preparation method below 90 °C.

The peak at 584 cm^{-1} assigned to Fe–O group (Lim *et al.* 2009) for MP and MOP indicates the presence of Fe oxide. FT-IR analysis shows the successful binding of Fe_3O_4 to OP surface groups. The characteristic intense absorption peak of OP at 3,418 cm^{-1} (O–H stretch) becomes a significant broad absorption from almost 3,620 cm^{-1} to 2,500 cm^{-1} in the MOP infrared spectrum, which indicates the existance of intramolecular free hydroxyl group (3,650–3,580 cm^{-1}) and the possible complexation interaction between Fe_3O_4-NPs and hydroxyl groups (3,400–3,200 cm^{-1}), carboxyl hydroxyl groups (3,200–2,500 cm^{-1}) of OP during the formation of MOP.

Figure 4(a) shows the TGA curves of MOP and OP in air. The weight loss in Process I can be attributed to the water desorption in MOP and OP samples below 120 °C. The total weight loss percentage is about 2.35% for MOP and 5.0% for OP, but the derivative thermogravimetry (DTG) peak of MOP appears at lower temperatures compared with OP, as shown in Figure 4(b) Section I. The intermolecular force between hydroxyl groups and water in OP seems to be more stable than that in MOP due to its possible complexation interaction of hydroxyl groups and Fe oxide.

According to their DTG curves in Figure 4(b) Section II and III, it is evident that both MOP and OP contain two oxidation processes: Process II begins at 121 °C and is mainly caused by intramolecular dehydration, dissociation and oxidation of hemicellulose and cellulose; Process III begins at 293 °C, which is mainly caused by combustion and carbonization of lignin (Zapata *et al.* 2009). In Process II, MOP shows better thermal stability than OP due to its DTG peak at a higher temperature, which indicates the binding force stabilization in the composite. Subsequently, the DTG peaks of MOP and OP appear nearly at the same temperature in Process III. The MOP and OP have the same thermal weight loss mechnism in Process III because the composite binding of OP and Fe oxide has been destroyed in this condition. Finally, the total weight loss percentage reaches up to 18.7% for MOP and 68.9% for OP at nearly 510 °C. There is a broad weight loss peak above 510 °C in the MOP DTG curve, which is probably attributed to the reaction between Fe oxide with pyrolytic carbon at high temperatures (Liu *et al.* 2018).

The weight loss of MOP is mainly attributed to OP oxygenolysis under the same decomposition condition and binding force between magnetite and OP is not considered. The apparent P value (magnetite weight percentage of MOP) can be obtained by Equation (2):

$$P_{Fe_3O_4} = 1 - \frac{1 - P_{MOP}}{1 - P_{OP}} \tag{2}$$

where P_{MOP} is the residual weight percentage of MOP and P_{OP} is the residual weight percentage of OP at the same temperature with the similar heating rate.

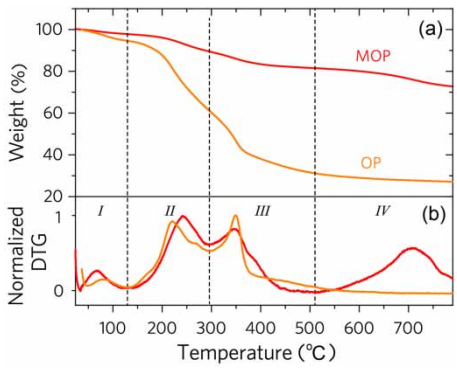

Figure 4 | (a) TGA curves of OP and MOP exhibiting thermal weight loss curve in air from room temperature to nearly 780 °C with a heating rate of 10 °C/min, (b) normalized DTG curves of OP and MOP with normalized weight loss rate versus temperature.

Downloaded from http://iwaponline.com/wst/article-pdf/84/1/159/913098/wst084010159.pdf
by guest

In Figure 5, the obtained apparent *P* value increases as the temperature rises from 150 °C up to 240 °C, which indicates that the thermal weight loss rate of MOP is lower than that of OP at the same temperature in first stage of Process II. It is worth noting that the apparent *P* value almost retains a constant value of 72.5% in the second half of Process II and in the whole Process III. This proves to be consistent with the previous hypothesis for this situation. The apparent *P* value decreases as the reaction between Fe oxide with pyrolytic carbon begins above 510 °C. The Fe content of the MOP was found to be 55.0% by inductively coupled plasma optical emission spectroscopy (ICP–OES) analysis (76.0% for Fe_3O_4 in MOP), which is similar to the above constant value of 72.5%.

To further identify the chemical characteristics of MOP, XPS analysis was performed and is shown in Figure 6. According to its wide-scan XPS spectrum (Figure 6(a)), MOP mainly consists of C, O, N, and Fe (H is not active for XPS analysis). According to C1s patterns of XPS in Figure 6(b), this peak can be divided into three simulated peaks of 284.7, 286.3 and 288.3 eV, which are assigned to the C in C–C, C–O and C = O, respectively. For the O1s, patterns of XPS are also divided into three simulated peaks as shown in Figure 6(c). The peak at 529.9 eV is attributed to lattice oxygen (O^{2-}) of Fe_3O_4-NPs. The peak at 531.4 eV is assigned to the O in hydroxyl groups (O–H). The peak of 532.7 eV may refer to the O in the oxygen bound species of C–O. The Fe2p peak can be further divided into eight peaks (Figure 6(d)), of which four simulated peaks at 710.1, 711.3, 723.0 and 724.6 eV are attributed to Fe^{2+}2p3/2, Fe^{3+}2p3/2, Fe^{2+}2p1/2 and Fe^{3+}2p1/2 and the other four peaks (grey lines) are assigned to the satellite peaks of Fe^{2+} or Fe^{3+} (Hu & Srinivasan 1999; Bhargava *et al.* 2007; Wilson & Langell 2014). These results show that the MOP catalyst contains Fe^{2+} and Fe^{3+} species (Fe^{3+}/Fe^{2+} peak area ratio is 2:1), which is consistent with the XRD results.

To quantitatively study the magnetic property of MOP, the magnetization curve was measured using vibrating sample magnetometry (VSM) at room temperature. The hystersis loop of MOP at 27 °C is shown in Figure 7(a). The saturation magnetization of MOP is around 61.5 emu/g with a ultralow coercivity force of nearly 43 Oe, indicating the MOP exhibits a superparamagnetic property (Wei *et al.* 2012). MOP can be attracted easily by a magnet and removed from water within 1 min (Figure 7(b)), which is a simple and fast method for rapidly magnetically separating and recovering a catalyst from a Fenton reaction system. Therefore, MOP is a promising candidate for an efficient and cost-saving alternative Fenton-like catalyst for practical application.

Catalytic removal of MO

To evaluate the catalytic degradation of MO under different conditions in a Fenton-like system, the following situations should be considered: (1) reaction with only MOP catalyst and without H_2O_2 (black diamond); (2) reaction with only H_2O_2 and without MOP catalyst (red dot); (3) reaction with both MOP catalyst and H_2O_2 (blue triangle). As shown in Figure 8(a), MO is non-degradable with only MOP added at 40 °C for 120 min, when there is a slight absorption of MO by MOP (around 4% within 2 h). When only H_2O_2 is added, the degradation ratio of MO is about 8% within 2 h, which is attributed to the lack of ·OH originating from the H_2O_2 without catalyst. It barely promotes the degradation of MO. Specifically, when MOP and H_2O_2 are simultaneously added, the efficiency of catalytic removal of MO reaches nearly 98% within 60 min and the aqueous solution in the reactor becomes nearly colourless.

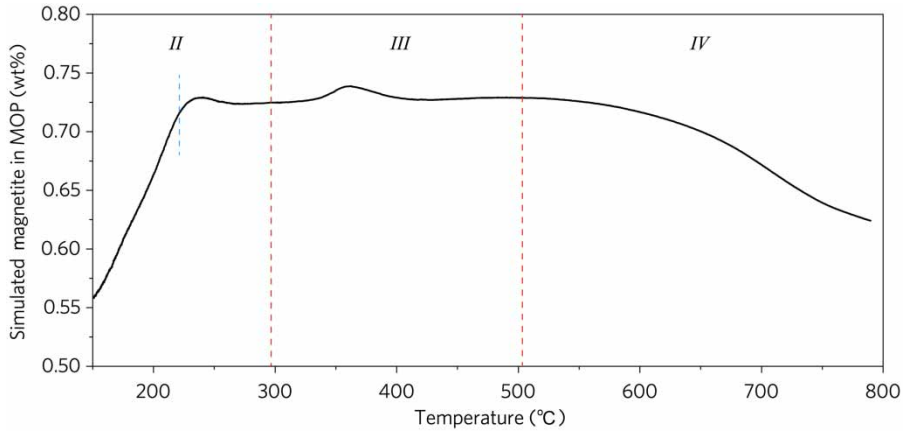

Figure 5 | The simulated magnetite content in MOP as a function of temperature at 10 °C/min heating rate.

Downloaded from http://iwaponline.com/wst/article-pdf/84/1/159/913098/wst084010159.pdf
by guest

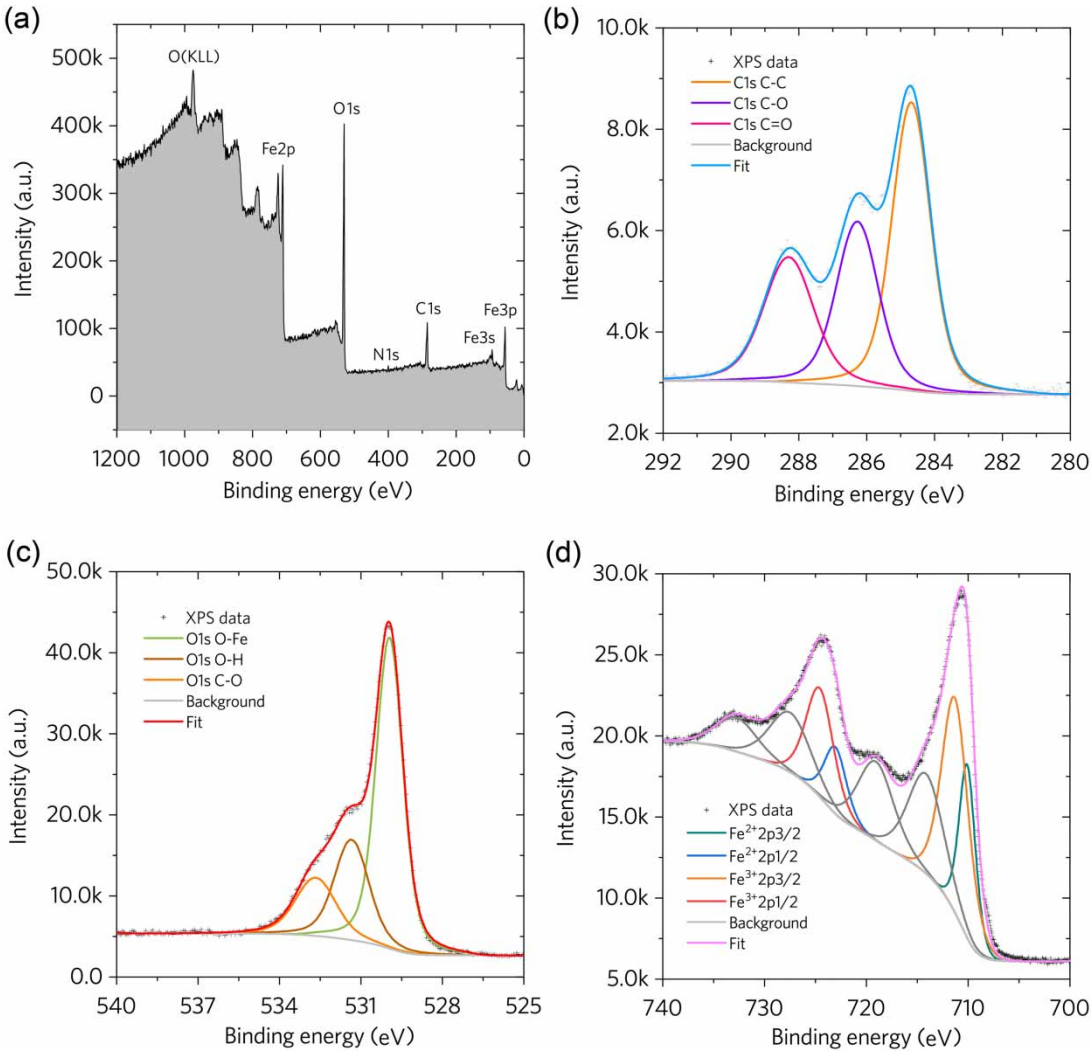

Figure 6 | (a) The wide-scan XPS spectrum of MOP, (b) the high-resolution C1s XPS spectrum, (c) the high-resolution O1s XPS spectrum and (d) the high-resolution Fe2p XPS spectrum of MOP.

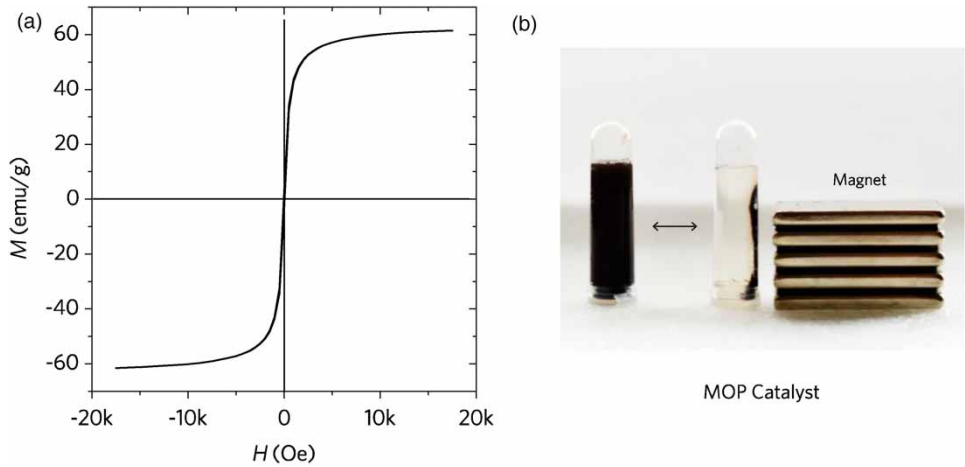

Figure 7 | (a) VSM curve of MOP catalyst at room temperature, (b) separation of MOP with a magnet within 1 min in aqueous solution system.

Downloaded from http://iwaponline.com/wst/article-pdf/84/1/159/913098/wst084010159.pdf
by guest

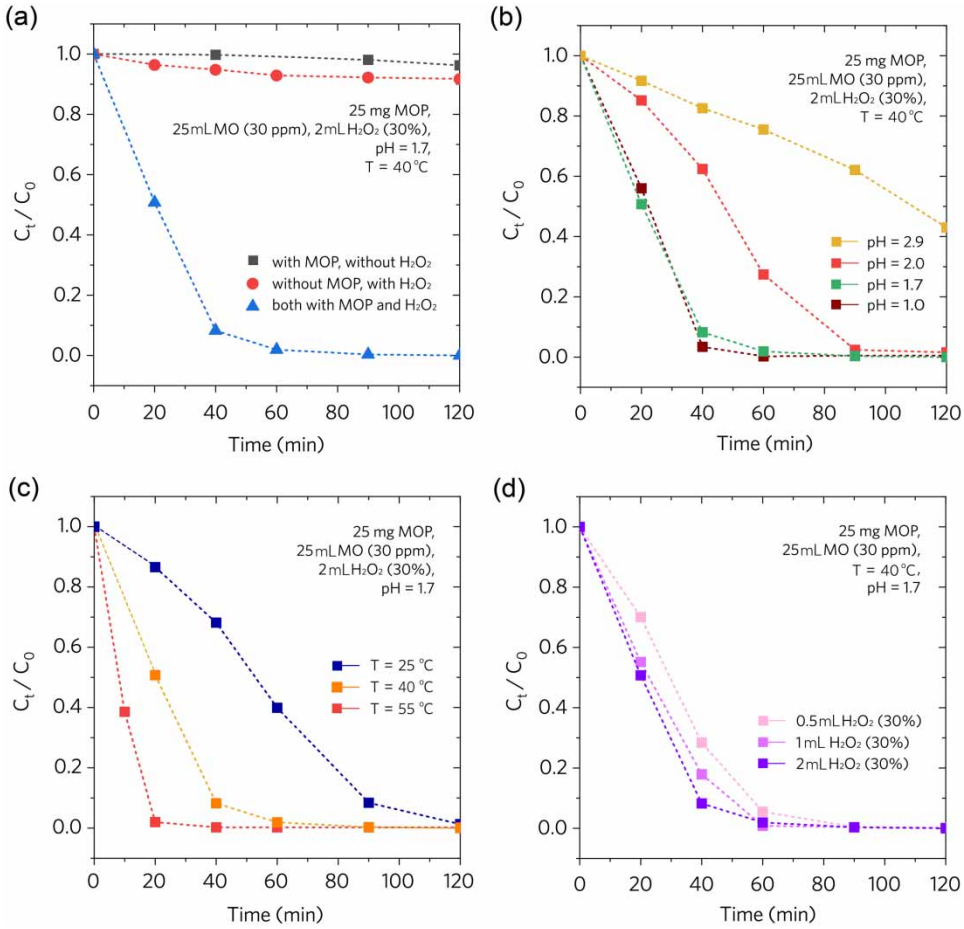

Figure 8 | (a) The degradation ratio of MO as a function of the reaction time in different conditions for heterogeneous Fenton-like catalytic systems, (b) degradation ratio of MO versus reaction time at different pH values, (c) degradation ratio of MO versus reaction time at different temperatures and (d) degradation ratio of MO versus reaction time with different H_2O_2 dosages.

The initial MO concentration is usually considered as one of the most critical factors affecting its degradation ratio. To elucidate the importance of initial dye concentration, 25 mL of 10, 20 and 30 ppm MO effluent solutions were investigated as shown in Figure A.5. The degradation ratio of MO decreases as the initial MO concentration increases. As the degradation of MO was increased by the MOP catalyst in the heterogeneous Fenton-like reaction, the percentages of the MO residue decreased to 50.7% (30 ppm), 18.6% (20 ppm) and 8.8% (10 ppm) within 20 min. More than 98% degradation ratio of MO within 60 min was observed for all three experimental conditions. The results indicate that the amount of ·OH generated by the MOP/H_2O_2 Fenton-like process in this condition is sufficient for high concentrations of up to 30 ppm of MO dye. More detailed reaction conditions like pH value, temperature and H_2O_2 dosage were subsequently investigated in this work.

The influence of pH on the degradation ratio of MO induced by the MOP catalyst is shown in Figure 8(b). It is observed that MO degradation ratio increases when the pH value changes from 3 to 1. Generally, MO degradation occurrs preferentially in an acidic condition for Fenton-like system. It has been reported that a very low pH restrains the degradation ratio of MO due to OH inactivation caused by hydrogen ion and dissolution of magnetite (Jia *et al.* 2019). Although the initial pH of 1 has shown better degradation in this reaction, it is likely because of protonation of abundant hydroxyl groups in the MOP which prevents the combination of H^+ and ·OH. Therefore, the MO degradation ratio at pH = 1.7 is almost 91.7% compared to with 96.6% for pH = 1.0 within 40 min. A pH of 1.7 was chosen as the optimum pH condition for later degradation experiments.

Figure 8(c) shows the degradation ratio of MO at different temperatures. The MO degradation ratio increases from 13.4% to 98.0% within 20 min reaction time when the temperature increases from 25 °C to 55 °C at pH of 1.7. It has been proven that

Downloaded from http://iwaponline.com/wst/article-pdf/84/1/159/913098/wst084010159.pdf
by guest

the enthalpy of the MO oxidative degradation is positive, which indicates that this process is endothermic. Therefore, the increase of temperature is beneficial to the degradation of MO for this heterogeneous Fenton-like reaction. However, the higher temperature needs more energy comsumption. Hence, the applicable temperature is considered to be 40 °C in this article.

The effects of the H_2O_2 dosage on the decomposition of MO was investigated at different volumes of H_2O_2 being 0.5, 1 and 2 mL. Figure 8(d) shows that the degradation ratio of MO increased from 71.6% to 91.7% within 40 min. This is probably because more H_2O_2 facilitates the increase of MO (30 ppm) degradation ratio. However, overdosed H_2O_2 does not significantly promote the degradation of MO but rather leads to a wastage of oxidizing agent (Jia *et al.* 2019; Zhu *et al.* 2019).

It is well known that the ·OH and hydroxyl oxygen radicals (·OOH) are generated in the heterogeneous Fenton-like catalytic degradation of organics. To evaluate the role of radicals on Fenton-like mechanisms, ethanol and chloroform are used to serve as scavengers for ·OH radicals and ·OOH radicals, respectively. The first-order kinetic simulations of Fenton-like degradation of MO (30 ppm of 25 mL) with no scavenger, ethanol (~18 mmol) and chloroform (~18 mmol) were investigated at pH = 1.7, 40 °C, 2 mL H_2O_2 (~18 mmol) and additive amount of 25 mg MOP catalyst. The results show that the kinetic constants are 0.061 min^{-1}, 0.038 min^{-1} and 0.025 min^{-1} (Figure A.6), which indicates both ·OH and ·OOH radicals play important roles in the decomposition of MO at this stage.

Cycle stability of MOP catalyst for degradation of MO

To evaluate the stability of the MOP catalyst, cycle experiments of the catalytic degradation of MO were performed in 10 runs (MP as the control group). To maintain a constant amount of Fe oxide for catalytic degradation, 30 mg of MOP and 22 mg of MP were added to 25 mL MO solution (20 ppm) with 2 mL dosage of H_2O_2 (30%) at pH 1.7 and 55 °C. In this situation, each cycle lasted 20 min and the degradation ratio of MO was measured. At the end of each cycle, the used catalyst was magnetically separated and then washed twice with deionized water in an oscillating manner.

As shown in Figure 9, MOP shows a better cycle stability than MP after 10 cycles. In the fifth cycle, MP catalytic degradation ratio decreases to less than 90%. By contrast, nearly 90% degradation ratio can be obtained for MOP in the 10th cycle, whereas MP shows only 62.5% in this stage. According to SEM images of the original and recycled MOP (after 10 cycles) in Figure A.7, there is no obvious change in their microstructure and morphology. It is evident that the magnetite crystal structure remains unchanged according to their XRD patterns of MOP before and after catalytic reaction (Figure A.8).

In addition, the FT-IR spectra of original MOP and recycled MOP (10 cycles) indicate that the main chemical groups of MOP do not changed after 10 cycles, as shown in Figure A.9. A slight decrease of infrared absorption peaks at 1,651 cm^{-1} (C = C) 1,384 cm^{-1} (O–H) and 1,071 cm^{-1} (C–O–C) suggests that the benzene ring (lignin) and glycosidic bond (cellulose and hemicellulose) structures are partially damaged by oxidative ·OH in the catalytic Fenton process, which shows the sacrificial role of OP in MOP (Zubir *et al.* 2015). According to ICP-OES analysis (Table A.4), the Fe content of MOP increases from 55.0% (initial) to 66.6% (after five cycles catalysis) because the OP decomposition is greater than Fe

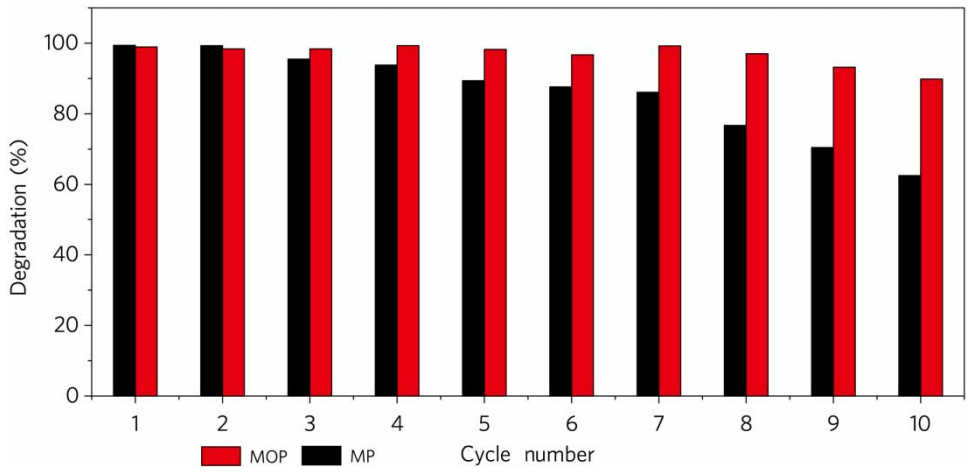

Figure 9 | Degradation ratio comparison between MOP and MP for the removal of MO in 10 cycles.

Downloaded from http://iwaponline.com/wst/article-pdf/84/1/159/913098/wst084010159.pdf
by guest

leaching at this stage. The Fe content decreases to 61.0% after 10 cycles catalysis due to the increase in Fe leaching. All results demonstrate that the synthesized MOP is an excellent long cyclic stable heterogeneous Fenton-like catalyst.

CONCLUSIONS

MOP is fabricated by one-step in-situ co-precipitation method, which exhibits a high catalytic efficiency, superparamagnetic property and good catalytic stability for the degradation of MO by a heterogeneous Fenton-like reaction. The degradation ratio of MO (30 ppm for 25 mL) is 98.0% within 20 min at pH 1.7, 55 °C, 2 mL H_2O_2 and 25 mg MOP. MOP also demonstrates good cycle catalytic stability over 10 cycles, with nearly 90% of degradation ratio of MO (20 ppm). This is probably because of the sacrificial role of biomass (OP) in MOP during the Fenton-like reaction, which slows down the dissolution of iron from the solid-state catalyst. All these results indicate that the MOP is a potential heterogeneous Fenton-like catalyst for azo dye wastewater treatment.

ACKNOWLEDGEMENTS

This work was financially supported by the Fundamental Research Funds for the Central Universities (project no. 3122019153) and Scientific Research Initial Foundation of Civil Aviation University of China (project no. 2020KYQD95).

DECLARATION OF INTEREST CONFLICTS

The authors declare no conflict of interest.

DATA AVAILABILITY STATEMENT

All relevant data are included in the paper or its Supplementary Information.

REFERENCES

Abboud, M., Youssef, S., Podlecki, J., Habchi, R., Germanos, G. & Foucaran, A. 2015 Superparamagnetic Fe_3O_4 nanoparticles, synthesis and surface modification. *Materials Science in Semiconductor Processing* **39**, 641–648.

Abdul-Hameed, H. M. & Al Juboury, M. F. 2020 MgFe-doubled layers hydroxide intercalated with low cost local adsorbent using for removal of lead from aqueous solution. *Journal of Water and Land Development* **45**, 10–18.

Adyani, S. H. & Soleimani, E. 2019 Green synthesis of Ag/Fe_3O_4/RGO nanocomposites by *Punica granatum* peel extract: catalytic activity for reduction of organic pollutants. *International Journal of Hydrogen Energy* **44** (5), 2711–2730.

Ahsan, M. A., Deemer, E., Fernandez-Delgado, O., Wang, H., Curry, M. L., El-Gendy, A. A. & Noveron, J. C. 2019a Fe nanoparticles encapsulated in MOF-derived carbon for the reduction of 4-nitrophenol and methyl orange in water. *Catalysis Communications* **130**, 105753.

Ahsan, M. A., Fernandez-Delgado, O., Deemer, E., Wang, H., El-Gendy, A. A., Curry, M. L. & Noveron, J. C. 2019b Carbonization of Co-BDC MOF results in magnetic C@ Co nanoparticles that catalyze the reduction of methyl orange and 4-nitrophenol in water. *Journal of Molecular Liquids* **290**, 111059.

Ahsan, M. A., Jabbari, V., El-Gendy, A. A., Curry, M. L. & Noveron, J. C. 2019c Ultrafast catalytic reduction of environmental pollutants in water via MOF-derived magnetic Ni and Cu nanoparticles encapsulated in porous carbon. *Applied Surface Science* **497**, 143608.

Ahsan, M. A., Jabbari, V., Imam, M. A., Castro, E., Kim, H., Curry, M. L., Valles-Rosales, D. J. & Noveron, J. C. 2020a Nanoscale nickel metal organic framework decorated over graphene oxide and carbon nanotubes for water remediation. *Science of the Total Environment* **698**, 134214.

Ahsan, M. A., Santiago, A. R. P., Nair, A. N., Weller, J. M., Sanad, M. F., Valles-Rosales, D. J., Chan, C. K., Sreenivasan, S. & Noveron, J. C. 2020b Metal-organic frameworks-derived multifunctional carbon encapsulated metallic nanocatalysts for catalytic peroxymonosulfate activation and electrochemical hydrogen generation. *Molecular Catalysis* **498**, 111241.

Ahsan, M. A., Santiago, A. R. P., Rodriguez, A., Maturano-Rojas, V., Alvarado-Tenorio, B., Bernal, R. & Noveron, J. C. 2020c Biomass-derived ultrathin carbon-shell coated iron nanoparticles as high-performance tri-functional HER, ORR and Fenton-like catalysts. *Journal of Cleaner Production* **275**, 124141.

Ahsan, M. A., Santiago, A. R. P., Sanad, M. F., Weller, J. M., Fernandez-Delgado, O., Barrera, L. A., Maturano-Rojas, V., Alvarado-Tenorio, B., Chan, C. K. & Noveron, J. C. 2021 Tissue paper-derived porous carbon encapsulated transition metal nanoparticles as advanced non-precious catalysts: carbon-shell influence on the electrocatalytic behaviour. *Journal of Colloid and Interface Science* **581**, 905–918.

Ali, I., Alharbi, O. M., Alothman, Z. A., Badjah, A. Y. & Alwarthan, A. 2018 Artificial neural network modelling of amido black dye sorption on iron composite nano material: kinetics and thermodynamics studies. *Journal of Molecular Liquids* **250**, 1–8.

Ali, I., Alharbi, O. M., ALOthman, Z. A., Alwarthan, A. & Al-Mohaimeed, A. M. 2019 Preparation of a carboxymethylcellulose-iron composite for uptake of atorvastatin in water. *International Journal of Biological Macromolecules* **132**, 244–253.

Downloaded from http://iwaponline.com/wst/article-pdf/84/1/159/913098/wst084010159.pdf
by guest

Al Juboury, M. & Abdul-Hameed, H. 2019 Using of activated carbon derived from agriculture waste coating by layered double hydroxide for copper adsorption. *Iraqi Journal of Agricultural Science* **50** (5), 1446–1454.

Alqadami, A. A., Naushad, M., ALOthman, Z. A., Alsuhybani, M. & Algamdi, M. 2020 Excellent adsorptive performance of a new nanocomposite for removal of toxic Pb(II) from aqueous environment: adsorption mechanism and modeling analysis. *Journal of Hazardous Materials* **389**, 121896.

Angamuthu, M., Satishkumar, G. & Landau, M. V. 2017 Precisely controlled encapsulation of Fe_3O_4 nanoparticles in mesoporous carbon nanodisk using iron based MOF precursor for effective dye removal. *Microporous and Mesoporous Materials* **251**, 58–68.

Babuponnusami, A. & Muthukumar, K. 2014 A review on Fenton and improvements to the Fenton process for wastewater treatment. *Journal of Environmental Chemical Engineering* **2** (1), 557–572.

Bhargava, G., Gouzman, I., Chun, C. M., Ramanarayanan, T. A. & Bernasek, S. L. 2007 Characterization of the 'native' surface thin film on pure polycrystalline iron: a high resolution XPS and TEM study. *Applied Surface Science* **253** (9), 4322–4329.

Chan, S. H. S., Yeong Wu, T., Juan, J. C. & Teh, C. Y. 2011 Recent developments of metal oxide semiconductors as photocatalysts in advanced oxidation processes (AOPs) for treatment of dye waste-water. *Journal of Chemical Technology & Biotechnology* **86** (9), 1130–1158.

Chen, B. L., Chen, Z. M. & Lv, S. F. 2011 A novel magnetic biochar efficiently sorbs organic pollutants and phosphate. *Bioresource Technology* **102** (2), 716–723.

Cheng, M., Zeng, G., Huang, D., Lai, C., Xu, P., Zhang, C. & Liu, Y. 2016 Hydroxyl radicals based advanced oxidation processes (AOPs) for remediation of soils contaminated with organic compounds: a review. *Chemical Engineering Journal* **284**, 582–598.

Cui, Z. M., Chen, Z., Cao, C. Y., Jiang, L. & Song, W. G. 2013 A yolk-shell structured Fe_2O_3@mesoporous SiO2 nanoreactor for enhanced activity as a Fenton catalyst in total oxidation of dyes. *Chemical Communications* **49** (23), 2332–2334.

Deng, Y. & Zhao, R. 2015 Advanced oxidation processes (AOPs) in wastewater treatment. *Current Pollution Reports* **1** (3), 167–176.

Du, D., Shi, W., Wang, L. Z. & Zhang, J. L. 2017 Yolk-shell structured Fe_3O_4@void@TiO_2 as a photo-Fenton-like catalyst for the extremely efficient elimination of tetracycline. *Applied Catalysis B-Environmental* **200**, 484–492.

Fan, H.-L., Li, L., Zhou, S.-F. & Liu, Y.-Z. 2016 Continuous preparation of Fe_3O_4 nanoparticles combined with surface modification by L-cysteine and their application in heavy metal adsorption. *Ceramics International* **42** (3), 4228–4237.

Feng, N. C., Guo, X. Y., Liang, S., Zhu, Y. S. & Liu, J. P. 2011 Biosorption of heavy metals from aqueous solutions by chemically modified orange peel. *Journal of Hazardous Materials* **185** (1), 49–54.

Gamallo, M., Fernández, L., Vázquez-Vázquez, C., Fondado, A., Mira, J., Feijoo, G. & Moreira, M. T. 2018 Development of a novel magnetic reactor based on nanostructured Fe_3O_4@PAA as heterogenous Fenton catalyst. *Catalysts* **9** (1), 18.

Gupta, V. K. & Nayak, A. 2012 Cadmium removal and recovery from aqueous solutions by novel adsorbents prepared from orange peel and Fe_2O_3 nanoparticles. *Chemical Engineering Journal* **180**, 81–90.

Holzwarth, U. & Gibson, N. 2011 The Scherrer equation versus the 'Debye–Scherrer equation'. *Nature Nanotechnology* **6** (9), 534.

Hu, Z. & Srinivasan, M. P. 1999 Preparation of high-surface-area activated carbons from coconut shell. *Microporous and Mesoporous Materials* **27** (1), 11–18.

Jia, X., Chen, X., Liu, Y., Zhang, B., Zhang, H. & Zhang, Q. 2019 Hydrophilic Fe_3O_4 nanoparticles prepared by ferrocene as high-efficiency heterogeneous Fenton catalyst for the degradation of methyl orange. *Applied Organometallic Chemistry* **33** (4), e4826.

Khan, M. A., Alqadami, A. A., Otero, M., Siddiqui, M. R., Alothman, Z. A., Alsohaimi, I., Rafatullah, M. & Hamedelniel, A. E. 2019a Heteroatom-doped magnetic hydrochar to remove post-transition and transition metals from water: synthesis, characterization, and adsorption studies. *Chemosphere* **218**, 1089–1099.

Khan, M. A., Otero, M., Kazi, M., Alqadami, A. A., Wabaidur, S. M., Siddiqui, M. R., Alothman, Z. A. & Sumbul, S. 2019b Unary and binary adsorption studies of lead and malachite green onto a nanomagnetic copper ferrite/drumstick pod biomass composite. *Journal of Hazardous Materials* **365**, 759–770.

Khan, M. A., Alqadami, A. A., Wabaidur, S. M., Siddiqui, M. R., Jeon, B.-H., Alshareef, S. A., Alothman, Z. A. & Hamedelniel, A. E. 2020 Oil industry waste based non-magnetic and magnetic hydrochar to sequester potentially toxic post-transition metal ions from water. *Journal of Hazardous Materials* **400**, 123247.

Lafi, R., Rezma, S. & Hafiane, A. 2015 Removal of toluidine blue from aqueous solution using orange peel waste (OPW). *Desalination and Water Treatment* **56** (10), 2754–2765.

Li, X., Cui, K., Guo, Z., Yang, T., Cao, Y., Xiang, Y., Chen, H. & Xi, M. 2020 Heterogeneous Fenton-like degradation of tetracyclines using porous magnetic chitosan microspheres as an efficient catalyst compared with two preparation methods. *Chemical Engineering Journal* **379**, 122324.

Lim, S.-F., Zheng, Y.-M. & Chen, J. P. 2009 Organic arsenic adsorption onto a magnetic sorbent. *Langmuir* **25** (9), 4973–4978.

Liu, Y., Peng, Y., Zhang, T., Qiu, F. & Yuan, D. 2018 Superhydrophobic, ultralight and flexible biomass carbon aerogels derived from sisal fibers for highly efficient oil–water separation. *Cellulose* **25** (5), 3067–3078.

Lv, Q., Li, G., Sun, H. Y., Kong, L. H., Lu, H. & Gao, X. X. 2014 Preparation of magnetic core/shell structured gamma-Fe_2O_3@Ti-tmSiO_2 and its application for the adsorption and degradation of dyes. *Microporous and Mesoporous Materials* **186**, 7–13.

Naushad, M., Alqadami, A. A., AlOthman, Z. A., Alsohaimi, I. H., Algamdi, M. S. & Aldawsari, A. M. 2019a Adsorption kinetics, isotherm and reusability studies for the removal of cationic dye from aqueous medium using arginine modified activated carbon. *Journal of Molecular Liquids* **293**, 111442.

Downloaded from http://iwaponline.com/wst/article-pdf/84/1/159/913098/wst084010159.pdf
by guest

Naushad, M., Sharma, G. & Alothman, Z. A. 2019b Photodegradation of toxic dye using Gum Arabic-crosslinked-poly (acrylamide)/$Ni(OH)_2$/FeOOH nanocomposites hydrogel. *Journal of Cleaner Production* **241**, 118263.

Oliveira, J. M., e Silva, M. R. d. L., Issa, C. G., Corbi, J. J., Damianovic, M. H. & Foresti, E. 2020 Intermittent aeration strategy for azo dye biodegradation: a suitable alternative to conventional biological treatments? *Journal of Hazardous Materials* **385**, 121558.

Shehzad, K., Xie, C., He, J., Cai, X., Xu, W. & Liu, J. 2018 Facile synthesis of novel calcined magnetic orange peel composites for efficient removal of arsenite through simultaneous oxidation and adsorption. *Journal of Colloid and Interface Science* **511**, 155–164.

Siles, J. A., Vargas, F., Gutiérrez, M. C., Chica, A. F. & Martín, M. A. 2016 Integral valorisation of waste orange peel using combustion, biomethanisation and co-composting technologies. *Bioresource Technology* **211**, 173–182.

Tan, X.-f., Liu, Y.-g., Gu, Y.-l., Xu, Y., Zeng, G.-m., Hu, X.-j., Liu, S.-b., Wang, X., Liu, S.-m. & Li, J. 2016 Biochar-based nano-composites for the decontamination of wastewater: a review. *Bioresource Technology* **212**, 318–333.

Tang, J. & Wang, J. 2018 Fenton-like degradation of sulfamethoxazole using Fe-based magnetic nanoparticles embedded into mesoporous carbon hybrid as an efficient catalyst. *Chemical Engineering Journal* **351**, 1085–1094.

Tijani, J. O., Fatoba, O. O., Madzivire, G. & Petrik, L. F. 2014 A review of combined advanced oxidation technologies for the removal of organic pollutants from water. *Water, Air, & Soil Pollution* **225** (9), 2102.

Titirici, M. M., Thomas, A., Yu, S.-H., Müller, J.-O. & Antonietti, M. 2007 A direct synthesis of mesoporous carbons with bicontinuous pore morphology from crude plant material by hydrothermal carbonization. *Chemistry of Materials* **19** (17), 4205–4212.

Wan, D., Li, W., Wang, G. & Wei, X. 2016 Size-controllable synthesis of Fe_3O_4 nanoparticles through oxidation-precipitation method as heterogeneous Fenton catalyst. *Journal of Materials Research* **31** (17), 2608.

Wang, Q. & Yang, Z. 2016 Industrial water pollution, water environment treatment, and health risks in China. *Environmental Pollution* **218**, 358–365.

Wei, Y., Han, B., Hu, X., Lin, Y., Wang, X. & Deng, X. 2012 Synthesis of Fe_3O_4 nanoparticles and their magnetic properties. *Procedia Engineering* **27**, 632–637.

Wilson, D. & Langell, M. A. 2014 XPS analysis of oleylamine/oleic acid capped Fe_3O_4 nanoparticles as a function of temperature. *Applied Surface Science* **303**, 6–13.

Youssef, N. A., Shaban, S. A., Ibrahim, F. A. & Mahmoud, A. S. 2016 Degradation of methyl orange using Fenton catalytic reaction. *Egyptian Journal of Petroleum* **25** (3), 317–321.

Zapata, B., Balmaseda, J., Fregoso-Israel, E. & Torres-Garcia, E. 2009 Thermo-kinetics study of orange peel in air. *Journal of Thermal Analysis and Calorimetry* **98** (1), 309–315.

Zhang, S., Zhao, X., Niu, H., Shi, Y., Cai, Y. & Jiang, G. 2009 Superparamagnetic Fe_3O_4 nanoparticles as catalysts for the catalytic oxidation of phenolic and aniline compounds. *Journal of Hazardous Materials* **167** (1–3), 560–566.

Zheng, D., Pei, S., Geng, S. & Zhang, L. 2019 Synthesis of Fe–Fe_3O_4/rGO composite with heterostructure through room-temperature reduction as photo-Fenton catalyst. *Journal of Nanoscience and Nanotechnology* **19** (9), 5858–5863.

Zhu, Y., Zhu, R., Xi, Y., Zhu, J., Zhu, G. & He, H. 2019 Strategies for enhancing the heterogeneous Fenton catalytic reactivity: a review. *Applied Catalysis B: Environmental* **255**, 117739.

Zou, J., Chai, W., Liu, X., Li, B., Zhang, X. & Yin, T. 2016 Magnetic pomelo peel as a new absorption material for oil-polluted water. *Desalination and Water Treatment* **57** (27), 12536–12545.

Zubir, N. A., Yacou, C., Motuzas, J., Zhang, X., Zhao, X. S. & da Costa, J. C. D. 2015 The sacrificial role of graphene oxide in stabilising a Fenton-like catalyst GO–Fe_3O_4. *Chemical Communications* **51** (45), 9291–9293.

First received 6 March 2021; accepted in revised form 29 May 2021. Available online 9 June 2021

Downloaded from http://iwaponline.com/wst/article-pdf/84/1/159/913098/wst084010159.pdf
by guest